Journal of Catalysis 404 (2021) 634–646

Contents lists available at ScienceDirect

Journal of Catalysis

journal homepage: www.elsevier.com/locate/jcat

Mimicking industrial aging in fluid catalytic cracking: A correlative microscopy approach to unravel inter-particle heterogeneities

M. Gambino [a], A.E. Nieuwelink [a], F. Reints [a], M. Veselý [a], M. Filez [a], D. Ferreira Sanchez [b], D. Grolimund [b], N. Nesterenko [c], D. Minoux [c], F. Meirer [a,*], B.M. Weckhuysen [a,*]

[a] Inorganic Chemistry and Catalysis, Department of Chemistry, Utrecht University, Universiteitsweg 99, 3584 CG Utrecht, the Netherlands
[b] Swiss Light Source, Paul Scherrer Institute, Villigen, Switzerland
[c] Total Research and Technology Feluy, Seneffe, Belgium

ARTICLE INFO

Article history:
Received 8 May 2021
Revised 18 September 2021
Accepted 8 October 2021
Available online 18 October 2021

Keywords:
Fluid catalytic cracking
Catalyst deactivation
Artificial deactivation
Microscopy

ABSTRACT

Artificially mimicking aging of an equilibrium catalyst (ECAT) is an effective strategy to model the deactivation of a Fluid Catalytic Cracking (FCC) catalyst during refinery operations. Herein, we have used a correlative microscopy approach to unravel inter-particle spatial heterogeneities in artificially deactivated catalysts (DCATs) and compared them with a real-life ECAT containing on average 3800 ppm of Ni and 2300 ppm of V, and a set of density separated ECAT fractions. By doing so we could rationalize the effect of metal contaminants on catalyst acidity and pore accessibility. More specifically, the Fe, Ni, and V distributions were obtained using X-Ray Fluorescence (XRF), while Confocal Fluorescence Microscopy (CFM) after thiophene and Nile Blue A staining, respectively provided a visualization of Brønsted acid sites and accessibility distribution. We found that not only the metal poisons distribution, but also hydrothermal degradation, that affects ECATs dealumination and related acidity drop, need to be properly reproduced by artificial catalyst deactivation protocols. Fe contamination must also be taken into account since it affects matrix accessibility.

1. Introduction

Fluid Catalytic Cracking (FCC) is one of the main petrochemical technologies for the production of gasoline and base chemicals, such as propylene.[1–6] The FCC catalyst is a hierarchical heterogeneous catalyst, containing a microporous zeolite active phase (typically zeolite Y), with a high concentration of Brønsted acid sites. [1,7,8]. The microporous zeolite is incorporated in a meso- and macroporous γ-Al_2O_3-containing matrix, which makes reagents/products transport possible and pre-cracks larger feedstock molecules.[1,7,9] Other components, such as clay, are included in the catalyst as part of the matrix or binder. During the cracking reaction, FCC catalyst particles accumulate coke and metal poisons contained in the crude oil feedstock or coming from reactor contamination (i.e., Ni, Fe and V).[7,10–13] In particular, while V penetrates deeper in the catalyst body, Ni and Fe are usually deposited in a shell-like distribution and they mainly accumulate within the first 3–5 μm of the catalyst particle surface, irreversibly blocking pores with a consequent drop in catalyst accessibility, reduced molecular diffusion and enhancement in surface coke deposition. [10,11,13–21] Fe is not only deposited on the catalyst particles surface from reactor contamination, but it is also naturally found in the clay component of the catalyst, and therefore present in the whole catalyst body. Industrial FCC catalysts are characterized by a particle age distribution, due to the fact that a portion of the catalyst material is regularly replaced with fresh catalyst. For this reason, we refer to the FCC catalyst in the reactor as equilibrium catalyst or ECAT.[22] In order to increase propylene yield during the catalytic cracking reaction, additives containing zeolite ZSM-5 are used in the reactor.[23,24] In this case, the ZSM-5 zeolite is embedded in a mesoporous silica matrix and P is usually added to ZSM-5-silica particles in order to aid the conversion of heavier molecules.

The development of laboratory deactivation protocols that can simulate the industrially deactivated equilibrium catalyst (ECAT) in terms of poisoning metals distribution, pore blocking effects and zeolite/matrix crystallographic modifications, is relevant for optimizing refinery operations and helps in the rational design of methods to improve FCC catalyst resistance to metal deactivation.[25–27] Up to date, several methods for artificial FCC catalyst deactivation exist, leading to so-called laboratory-deactivated cat-

* Corresponding authors.
E-mail addresses: f.meirer@uu.nl (F. Meirer), b.m.weckhuysen@uu.nl (B.M. Weckhuysen).

https://doi.org/10.1016/j.jcat.2021.10.012
0021-9517/

alyst (DCATs) materials. Normally, lab testing of FCC catalysts involves catalyst metalation with Ni- and V-containing precursors and hydrothermal aging under reduction–oxidation environment. The latter aspect is important to mimic the effect of vanadium, which penetrates and destroys the zeolite much more effectively in the oxidation state +5. One of the most known FCC deactivation methods to introduce metals is Mitchell Impregnation (MI), where the FCC catalyst is impregnated with Ni- and V-organic precursors and subsequently exposed to a steaming treatment.[26,28] In order to mimic the reduction–oxidation environment, often a Cyclic Propylene Steaming (CPS) is used.[29,30] Since this deactivation method does not result in a Ni distribution similar to the one observed in an ECAT material due to a too high penetration of Ni in the catalyst particles during impregnation, other methods have been developed. For instance, Wallenstein et al. [30] have found that substituting Mitchell impregnation with spray impregnation leads after CPS to a Ni and V distribution that is more similar to the one observed for the ECAT. Previous EDX-SEM studies on cross sections of ECAT and catalysts that were artificially deactivated using Mitchell impregnation or spray impregnation in combination with CPS cycles, showed that spray impregnation better simulates Ni and V distributions of the ECAT in the FCC catalysts. In particular, in spray impregnated samples V penetrates deeper within the FCC catalyst particles only after CPS, while the distribution of V after Mitchell impregnation was already uniform before the CPS, with zeolite unit cell size after deactivation being similar to that of the ECAT sample. This showed that spraying the metals solutions in a FCC catalyst fluidized bed within a spray impregnation unit followed by CPS simulates fairly well the metals distributions occurring in the FCC unit.[30]

An alternative to metalation and CPS is Cyclic Deactivation (CD), that exposes the catalyst to several reaction cycles, mixing the feedstock with Ni and V naphtalenates.[25,27,31] Although the reaction conditions are similar to the riser reactor ones, this artificial deactivation protocol is not able to exactly reproduce real-life catalyst industrial deactivation.

It is important to note that Psarras et al.[27], amongst other researchers in academia and industry, have reported improved artificial deactivation protocols. The study showed that both catalysts, deactivated via improved CPS and CD, showed a more similar metal distribution as ECAT than conventional CPS and CD respectively, but were also more active. FTIR acidity measurements showed that the artificially deactivated samples maintained a higher concentration of acid sites compared to the ECAT.[27] Psarras et al. also showed in the same study the so-called Albemarle Accessibility Index (AAI) methodology, that tracks via UV–vis spectroscopy the diffusion of liquid large organic molecules in the absence of reaction. The authors report that the artificially deactivated samples showed a higher accessibility than the fresh samples, that they attribute to structural changes related to the porous network.[27] In a previous SEM-EDS study on CPS and CD, Psarras et al. [31] observed that while the ECAT samples formed upon aging phases containing Ni and Al, laboratory deactivated samples did not, and this was surely a limit of the artificial aging protocols.

The above discussed studies illustrate how difficult it is to fully reproduce the complex aging phenomena occurring in an industrial FCC riser-regenerator unit. There is clearly room for further improvements, in particular to simulate ECATs pore blocking and accessibility drops.

In order to understand if the artificial deactivation protocols can reproduce the main characteristics of the industrially deactivated FCC samples, it is necessary to choose an appropriate set of real-life ECAT references. To this end, comparing density sorted fractions of an ECAT sample would be ideal to assess the effects of hydrothermal degradation and metals mediated aging.[32] Density separation of the ECAT is usually achieved with a sink-flow method, where a solvent is used to separate the catalyst particles according to their metal content: the higher the metal content, the higher the density of the fraction and its catalytic age.

The use of Confocal Fluorescence Microscopy (CFM) in combination with probe molecules is a powerful tool in life sciences research to visualize cellular components by staining with fluorescent dyes that selectively react with a specific target.[33–36] This approach has been successfully used by our research group to track the acid site distribution in FCC catalysts.[32,35–42] Acid sites variations can be correlated with poisoning metals distribution that can be assessed on a laboratory base by using e.g., X-Ray Fluorescence Microscopy (μXRF). For example, Buurmans et al. have developed a staining procedure that allows to simultaneously stain the FCC catalyst single particle with thiophene and Nile Blue A, in order to respectively track Brønsted acid sites distribution and matrix accessibility by means of CFM.[36] In fact, the non-fluorescent thiophene molecule is small enough to diffuse into the zeolite domains and react with Brønsted acid sites, forming fluorescent oligomers. On the other hand, Nile Blue A can act as size-exclusion probe for particles accessibility: due to its size, this fluorescent molecule can diffuse through the meso- and macro-pores of the FCC catalyst matrix, but it cannot enter the zeolite micropores.[36] μXRF is an ideal tool for tracking poisoning metals distribution and has been recently used as poisoning metals screening tool in the development of a new method for magnetophoretic sorting of FCC catalyst particles in our group.[40] More recently, Nieuwelink et al. [32] have used staining with styrene (as acidity probe) and Nile Blue A (as accessibility probe) in combination with laboratory-based μXRF in order to study the complex mechanisms of ECAT deactivation at a multi-particle level.

The aim of this study is to compare poisoning metals distribution, catalyst acidity and accessibility in ECATs and DCATs, building on the knowledge developed by our research group during past studies of ECATs. One should mention here that the ECATs and the fresh FCC catalyst used to prepare the DCATs were sampled from the same industrial plant during the same period of operation thereby guaranteeing that a more reliable comparison between ECATs and DCATs can be made. The DCATs under analysis can be divided in two macro-groups, according to the artificial deactivation protocol used: D1, D2 and D3 were deactivated using a combination of metalation and CPS,[30] being the metalation method Mitchell impregnation for D1 and D2 and spray impregnation for D3, while D4 and D5 were subjected to a combination of CD and CPS. [29]

The ultimate goal of the current work is to optimize a correlative micro-spectroscopic approach to efficiently compare inter-particle heterogeneities related to catalyst deactivation in a real-life industrial ECAT and its density sorted fractions, with artificially deactivated catalysts (DCATs), to correlate in the same region of space, or region of interest (ROI), metals distribution, acidity and accessibility for the same set of particles. A Ni and V-rich unseparated ECAT material, that was exposed to non-hydrotreated feedstock (ECAT) will be analyzed as reference. Moreover, density separated fractions of the ECAT sample will also be studied in order to highlight the differences as the metals content varies. Hence, the aim of this study is to: i) assess poisoning metals distribution by using μXRF; ii) assess Brønsted acid sites distribution and particles accessibility by using CFM, after respectively staining with thiophene and Nile Blue A; iii) using statistical analysis to correlate spatial variations in acidity and accessibility with poisoning metals distribution; and iv) evaluate the fraction of additive particles containing zeolite ZSM-5, that are usually added to real-life FCC catalysts to enhance propylene yields and that usually have different matrix (therefore accessibility) properties. This will further help to highlight differences among DCATs deactivated with different

methods and to establish a robust and practically useful tool for the future development of laboratory-based deactivation protocols.

2. Materials and methods

An industrially deactivated unseparated ECAT – containing approximately 3800 ppm of Ni and 2300 ppm of V –, density separated [10] fractions of this ECAT further denoted as ECATa, ECATb, ECATc and ECATd) and laboratory-deactivated DCATs samples (further denoted as D1, D2, D3, D4 and D5, all containing a comparable amount of poisoning metals as the industrially obtained ECAT sample) were investigated in this study. Table 1 reports the metal contents of the unseparated ECAT and the DCATs. The unit cell size of zeolite Y within these samples was determined by X-ray Diffraction (XRD) according to the Standard ASTM D3942-97 procedure. Surface areas of the different catalyst materials were determined by nitrogen adsorption using a Micromeritics Tristar 3000 unit, while the zeolite (ZSA) and matrix (MSA) surface areas were calculated by the t-plot method.

2.1. Deactivation protocols

Simulation of the deactivation of an FCC catalyst that occurs in FCC units in the laboratory, is usually done via different accelerated aging protocols. A choice of the most appropriate protocol is far to be trivial. One of the challenges is how to properly mimic the effect of metals in an accelerated aging procedure. In this context, several different metal deposition techniques could be applied in combination of a standard aging procedures. The most known metalation techniques are based on Mitchell impregnation, deposition of metals by spay-impregnation and cracking of VGO doped with organic salts of V and Ni.

D1 and D2 were prepared using the Mitchell-type impregnation to introduce V and Ni on the catalysts.[30]

The only difference in preparations was in a pre-steaming of the D2 before impregnation to mimic the thermal choc at the exposition of a fresh catalyst to the hydrothermal environment in the regenerator of an FCC unit before the first contact with metal-containing feedstock. The hydrothermal treatment was performed by introducing the sample directly in the fluidized type of reactor at 700 °C for 30 min in 100% steam environment. A strategy behind was in decreasing of the reactivity of external surface before the impregnation with metals.

Metalation of the D3 was done using the spray-impregnation method.[30] The idea behind was in deposition of the metal mostly on outer surface of the FCC catalyst particles. After the impregnation, D1, D2 and D3 samples were subjected to CPS-3 standard deactivation procedure.[29]

The samples D4 and D5 were first hydrothermally deactivated at 780 °C in 100% of steam for 12 h and 32 h respectively. Then, both samples were subjected to 20 cycles of metal deposition by cracking of the VGO doped with V and Ni naphthenates at 540 °C and regeneration at 780 °C. After the metalation, both samples were subjected to the CPS – 3 type of aging.[29]

The same concentration targets of 3500 ppm of Ni and 2500 ppm of V were used in all metal-introduction procedures. The average metals levels determined by ICP analysis are reported in Table 1.

2.2. Catalytic performance

The catalytic properties of the samples were determined with an advanced cracking evaluation (ACE) unit[43] at five different catalyst-to-oil ratios (C/O) from 3.0 to 7.0 g/g and the reaction temperature 535 °C. The catalyst-to-oil ratios were varied by changing the mass of the catalyst whilst the total amount of feed and time-on-stream was kept constant. The data reported in this study were obtained from interpolations at iso- catalyst-to-oil ratio (*iso*-C/O) at constant conversion.

2.3. Correlative microscopy

Ex-situ staining was carried out using thiophene and Nile Blue A. A scheme explaining the staining protocol is shown in Fig. 1**a and b**. The FCC catalyst particles were first kept in contact with 15 μL of thiophene in a glass vial in order to favor the diffusion of the stain inside the catalyst porous network. Then, the mixture was transferred on a microscopy slide and the Brønsted acid sites catalyzed thiophene oligomerization reaction was ignited by heating for 10 s at 100 °C. Afterwards, the catalyst was transferred in another glass vial and put in contact for 1 h with 15 μL of Nile Blue A (solution in ethanol 0.1% vol) at room temperature. The solvent was then evaporated, and the catalyst particles were sprinkled on Kapton tape using a microscopy slide as support. A paper window having 0.5 cm diameter was applied on each microscopy slide, in order to have a homogeneous field of view.

Optical microscopy (OM) images were acquired using a Zeiss microscope, while CFM measurements were performed with a Nikon A1 confocal fluorescence microscope (10x objective) in DU4 mode and the same laser settings were used for all the samples. A 488 nm and 642 nm lasers were used to respectively excite thiophene oligomers and Nile Blue A in the same region of interest (ROI). The fluorescence emitted from the sample was measured in the spectral range 500–550 nm for thiophene oligomers and in the spectral range of 662–737 nm for Nile Blue A.

μXRF was measured with an Orbis PC SDD instrument, having a Rh-tube as X-ray source (40 kV and 200nA). FCC catalyst particles were scanned with a 30 μm beam, using a step size of 15 μm and 300 ms integration time. A full XRF spectrum per pixel was collected during these measurements. The PyMca software was used to carry out a batch fitting analysis of the μXRF dataset.[44] Fig. 1**c** shows a scheme of the correlative microscopy approach used in this study.

Table 1
Physical and chemical properties of the FCC catalyst materials under study: unit cell size (UCS); iron, lanthanum, nickel and vanadium average concentrations as determined by ICP analysis; total surface area (TSA), zeolite surface area (ZSA), matrix surface area (MSA), micropore volume (Vμ) and ZSA/MSA ratio.

	UCS (Å)	Fe ppm	La wt%	Ni (ppm)	V (ppm)	TSA (m^2/g)	ZSA (m^2/g)	MSA (m^2/g)	Vμ ml/g	ZSA/MSA
ECAT	24.302	3800	2.84	3800	2300	170	142	28	0.055	5.1
D1	24.305	2574	2.85	3200	2200	165	137	29	0.053	4.7
D2	24.307	2574	2.85	2500	2100	166	136	29	0.053	4.7
D3	24.295	2574	2.85	2950	2150	171	141	30	0.055	4.7
D4	24.345	2574	2.85	2799	1987	204	173	30	0.067	5.8
D5	24.324	2574	2.85	3097	1974	187	159	28	0.062	5.7

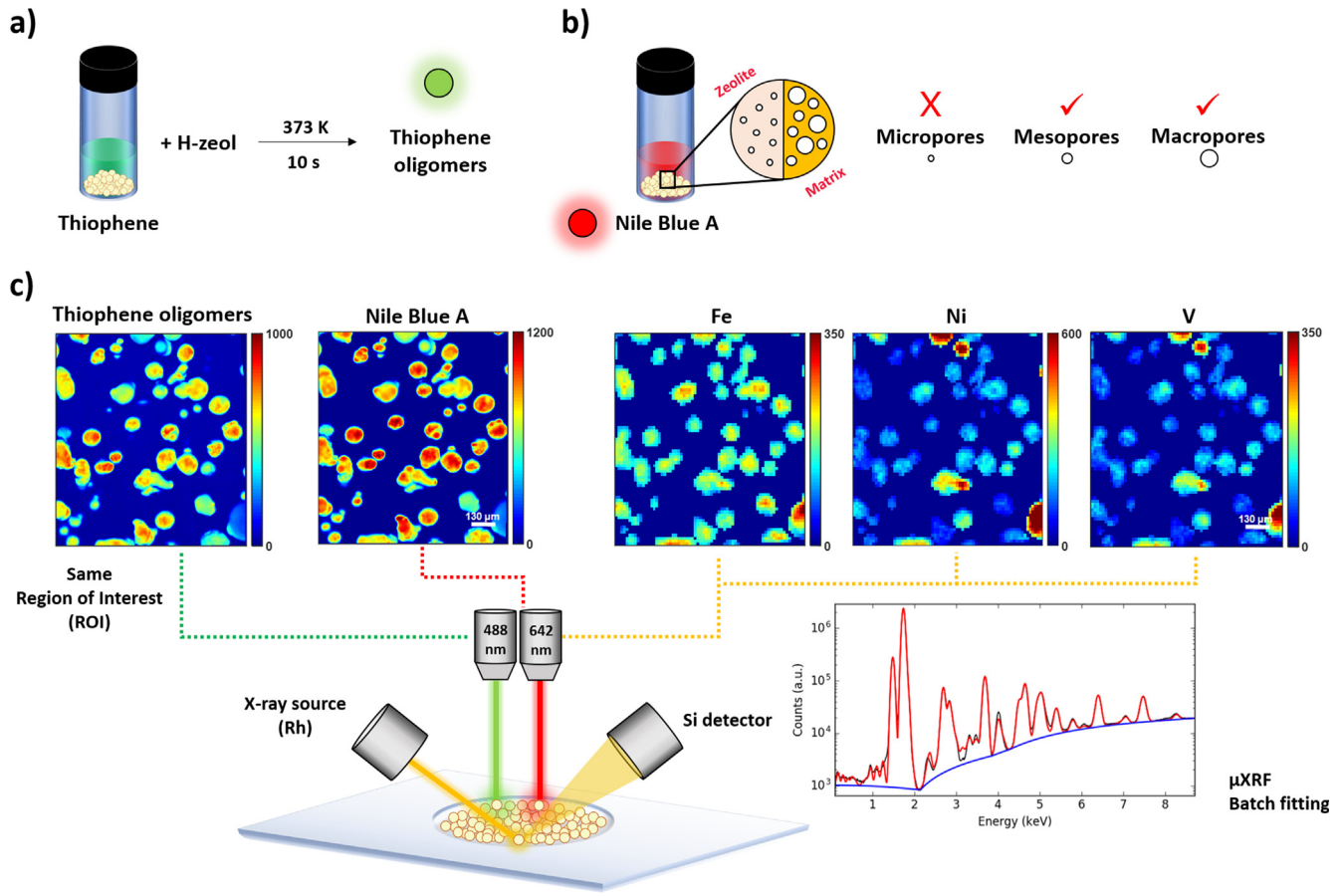

Fig. 1. Schematic view of the different staining and analytical methods used in this work for studying FCC materials: **a)** The thiophene oligomerization reaction was used as an analytical tool to display the Brønsted acid sites distribution; **b)** Nile Blue A was used as a size-exclusion probe to visualize particle accessibility. **c)** Experimental panel showing the correlative microscopy approach used in this work. FCC catalyst particles were characterized with Confocal Fluorescence Microscopy (CFM), using 488 nm and 642 nm lasers, to respectively excite thiophene oligomers and Nile Blue A. In the same spatial region, or Region-of-Interest (ROI), laboratory-based X-ray Fluorescence Microscopy (μXRF) was carried out using a Rh-source: a full XRF spectrum was collected for each pixel and the poisoning metals elemental distribution was retrieved through a batch fitting procedure.

2.4. X-ray diffraction – X-ray fluorescence tomography

μXRD/μXRF tomography measurements of the FCC additives particles (i.e., ECATd) were carried out at the Swiss Light Source (SLS) X05LA beamline. A virtual slice was measured by rotating the single particle between 0 and 180° (2° step size) and for each tomographic angle a line scan was collected, using 1×1 μm^2 beam size at 12.1 keV.

3. Results

3.1. Catalytic performance

The results of the catalytic tests performed, summarized in Fig. 2, Table 2 and Table 3 demonstrate a significant difference between the ECAT sample and the DCATs. The ECAT shows a significantly higher Liquefied Petroleum Gas (LPG) yield at the expense of gasoline production, which can be attributed to the presence of propylene additives in the catalyst batch (i.e., zeolite ZSM-5) that enhance the cracking activity of gasoline to LPG. Moreover, the low conversion and relatively high Light Cycle Oil (LCO) yield at *iso*-C/O could be attributed to diffusivity problems, caused by iron contamination of the ECAT. It was found that Fe is around 30% more concentrated on the ECAT compared to the corresponding DCATs (refer to Table 1). In both ECAT and DCATs Fe is naturally found in the clay component of the catalyst, and therefore present in the whole catalyst body, while in the ECAT only Fe is additionally deposited on the catalyst particles surface mainly from reactor contamination. The artificial aging protocols currently described in literature are mainly focused on simulating Ni and V contamination, but do not sufficiently address the issue of Fe poisoning. The DCAT materials of this study were not artificially impregnated with Fe to simulate the additional deposition of Fe on the catalyst surface. It is reasonable to think that iron-contamination may impact the diffusion of large molecules and prevent their cracking to gasoline.

Regarding DCATs, LPG yield is lower than ECAT and gasoline yield higher, due to the absence in the DCATs of ZSM-5 additives, while gasoline yield shows an inverted trend, with DCATs having higher yields than ECAT. The LCO yield at *iso*-C/O for DCATs is similar to ECAT and there are not big differences among DCATs deactivated with different methods. The most relevant difference among DCATs is in the conversion of D1, D2, D3 and D4, which is higher than in D5 and ECAT. D4 and D5 were hydrothermally deactivated at 780 °C in 100% steam for 12 and 32 h respectively and then deactivated with the same combination of CD and CPS. The similarity between D5 and ECAT conversion and their difference compared to D4 suggests that also hydrothermal degradation plays a key role in the catalytic activity during FCC. Therefore, this is a parameter to be taken into account when establishing artificial deactivation protocols.

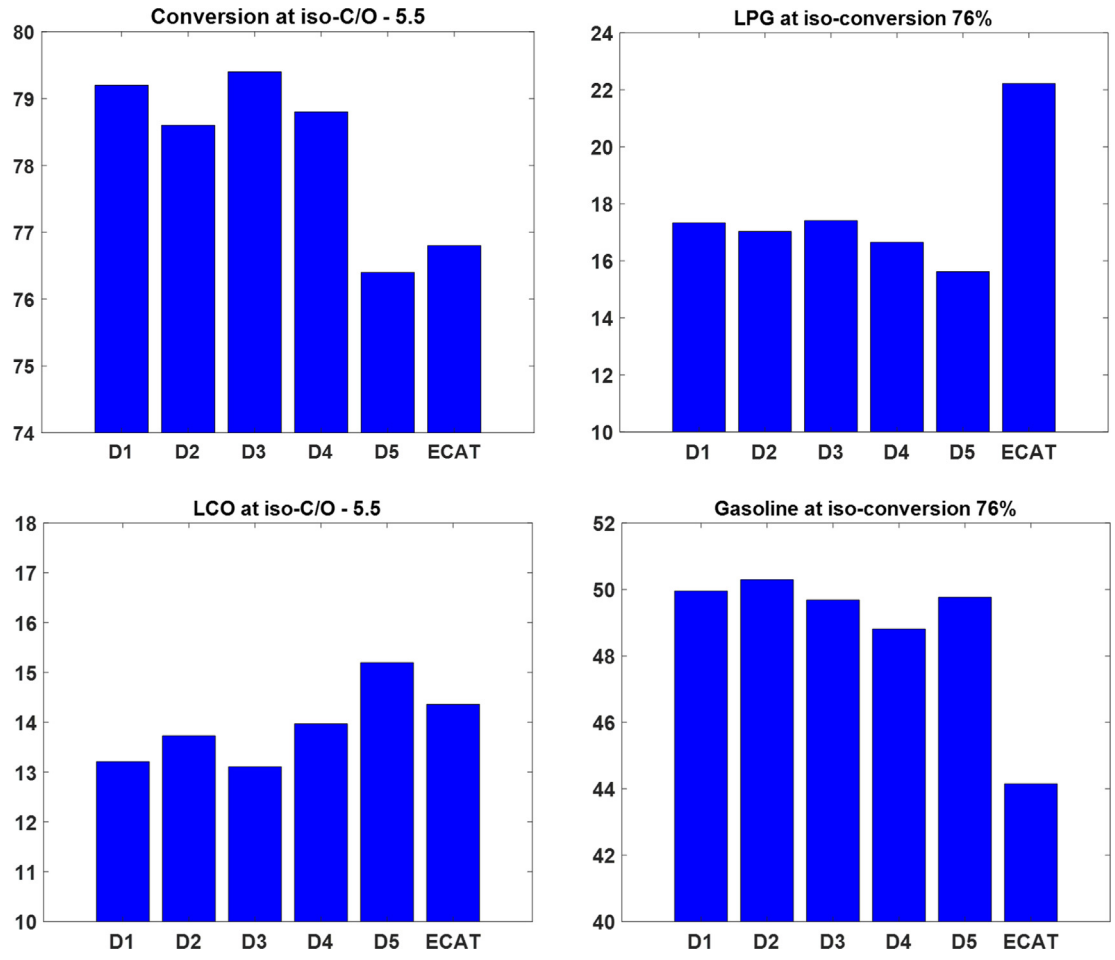

Fig. 2. Extrapolated catalyst performances of the ECAT and DCATs under study.

Table 2
Catalytic performance test results at *iso*-conversion.

CATALYST	D1	D2	D3	D4	D5	ECAT
Conversion	76	76	76	76	76	76
C/O	3.5	3.6	3.3	3.7	5.2	5.0
Dry gases	2.9	2.9	3.0	3.4	3.1	3.1
$\mathbf{C_3^=}$	1.4	1.3	1.5	1.4	1.1	1.8
$\mathbf{C_3^-}$	4.8	4.7	4.7	4.6	4.5	7.2
Total C_3	6.2	6.0	6.2	6.0	5.6	9.0
Total $C_4^=$	5.6	5.5	5.5	5.4	5.3	6.5
Total C_4	11.2	11.0	11.2	10.7	10.0	13.2
LPG	17.3	17.0	17.4	16.7	15.6	22.2
Gasoline	50.0	50.3	49.7	48.8	49.8	44.2
Coke	5.8	5.8	5.9	7.1	7.6	6.6
LCO	15.0	15.0	14.8	15.5	15.4	14.8

Moreover, D4 and D5 exhibit higher coke yields at *iso*-conversion compared to the ECAT (Table 2), D1, D2 and D3: coke yields at *iso*-conversion seem to be higher in the CD-CPS deactivated samples, that have higher TSA compared to ECAT, D1, D2 and D3 and that were subjected to a long hydrothermal deactivation treatment.

A significant difference in catalysts performance can be observed when considering different aging procedures, but these differences are not correlated with DCATs textural differences. For example, the D4 sample that shows very different textural characteristics compared to the other DCATs, having the highest TSA (Table 1), has more similar performance to the D1-D3 series than to the D5 sample, which looks more similar to D4 from textural results. This difference could be related to the fact that during BET measurements all the accessible surface in the particle contributes to the final surface area value, with no influence from diffusion. On the other end, during catalytic performance measurements, diffusion and feedstock residence time play an important role. This implies that the active sites that are far from the center of the catalyst particle contribute with higher turnovers compared to the active sites in the center. Specific diffusion measurement like AAI accessibility index or inverse GC tools should be used in this case. However, this type of measurements gives an average result that does not take into account the inter-particle heterogeneities of FCC catalyst. It is evident that only correlative analytical techniques may shed light on these differences

Table 3
Catalytic performance test results at *iso*-C/O.

CATALYST	D1	D2	D3	D4	D5	ECAT
Conversion	79.2	78.6	79.4	78.8	76.4	76.8
C/O	5.5	5.5	5.5	5.5	5.5	5.5
Total dry gases	3.2	3.1	3.3	3.1	3.7	3.2
C_3^+	1.6	1.5	1.7	1.5	1.1	1.9
$C_3^=$	5.2	5.0	5.1	4.9	4.5	7.2
Total C_3	6.8	6.5	6.8	6.4	5.6	9.1
Total $C_4^=$	5.7	5.6	5.5	5.4	5.4	6.5
Total C_4	12.2	11.9	12.2	11.3	10.2	13.4
LPG	19.0	18.4	19.0	17.7	15.8	22.4
Gasoline	49.4	49.8	49.1	49.7	48.4	44.3
Coke	7.8	7.4	8.1	9.0	7.8	7.0
LCO	13.2	13.7	13.1	14.0	15.2	14.4

in a spatially resolved way, overcoming the limitations of bulk techniques.

3.2. Metal poisons

Figs. 3 and 4 respectively show the Fe, Ni and V XRF maps for the ECAT and DCAT materials, while Fig. 5 summarizes the average poisoning metals distribution in the analyzed Region-of-Interest (ROI) (also refer to Figs. S4 and S5 for the average XRF counts per particle). It can be immediately observed that the non-hydrotreated unseparated ECAT sample shows inter-particle heterogeneities in Ni and V distribution (i.e., hotspots) and this is compatible with the age distribution of the FCC particles. Regarding Fe, the unseparated ECAT material shows the presence of Fe-rich catalyst particles: it is well known that Fe is naturally contained in the clay, but it is also accumulated from feedstock contamination and hardware corrosion in the reactor. We observe a heterogeneous distribution for this metal, that could be related to contamination both from crude oil feedstock and reactor components, which is in line with the higher amount of Fe contaminant found in the ECAT (~3800 ppm) sample compared to other samples (~2500 ppm).

ECATa, the fraction with the highest skeletal density, has the highest content of Fe, Ni and V and shows a high number of Ni-V hotspots, indicating the presence of catalytically old FCC particles. In the ECATb, ECATc and ECATd fractions, the concentration of Fe just slightly decreases, but it is still similar to the heaviest fraction ECATa. On the other hand, the Ni and V concentration in these samples decreases following the order: ECATd < ECATc < ECATb. Also, in the ECATc and ECATd samples we basically do not observe Ni and V hotspots (i.e., they have a more homogeneous low metal concentration).

Compared to the unseparated ECAT sample, the DCAT samples have quite a homogeneous Fe distribution, probably because the artificially deactivated samples did not accumulate additional Fe and therefore contain only that present in the clay. D1 has the most similar characteristics compared to the unseparated ECAT, in terms Ni and V hotspots. Also the D2 and D3 samples have a similar Ni and V distribution as ECAT, but the number of hotspots decreases compared to the D1 sample. Hence, there is the following order: D1 > D2 > D3. Finally, the D4 and D5 samples have a more homo-

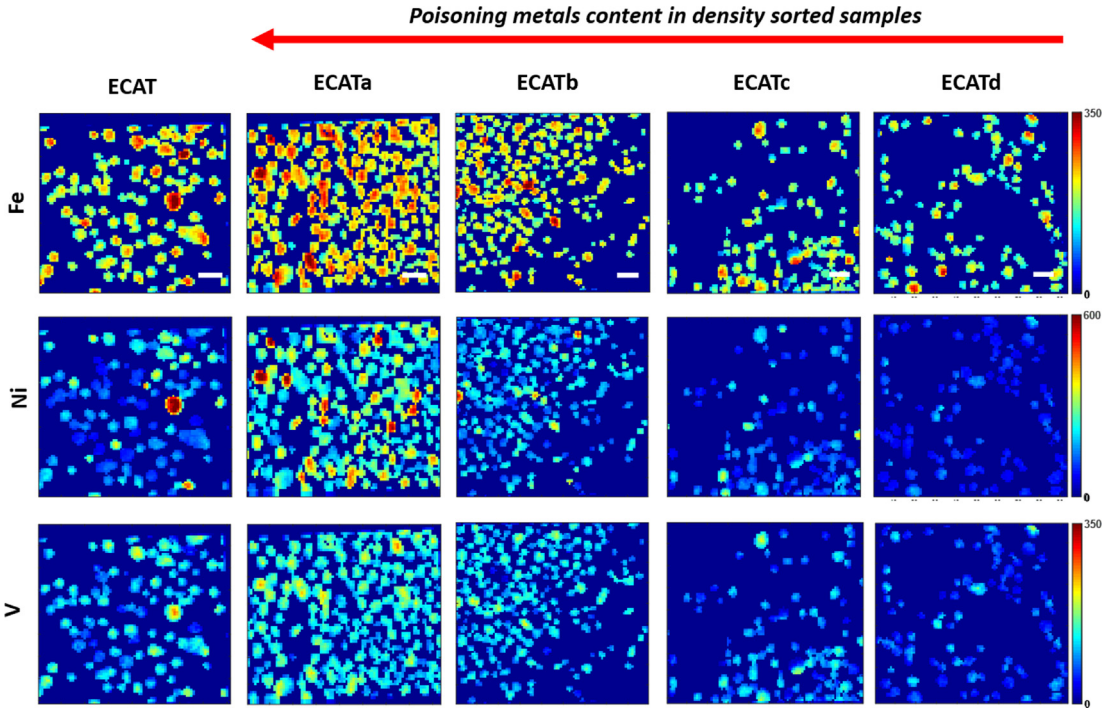

Fig. 3. Elemental distribution maps of Fe, Ni and V poisoning metals for the different ECATs samples, obtained after batch fitting analysis of the μXRF dataset. The scale bar indicates 150 μm.

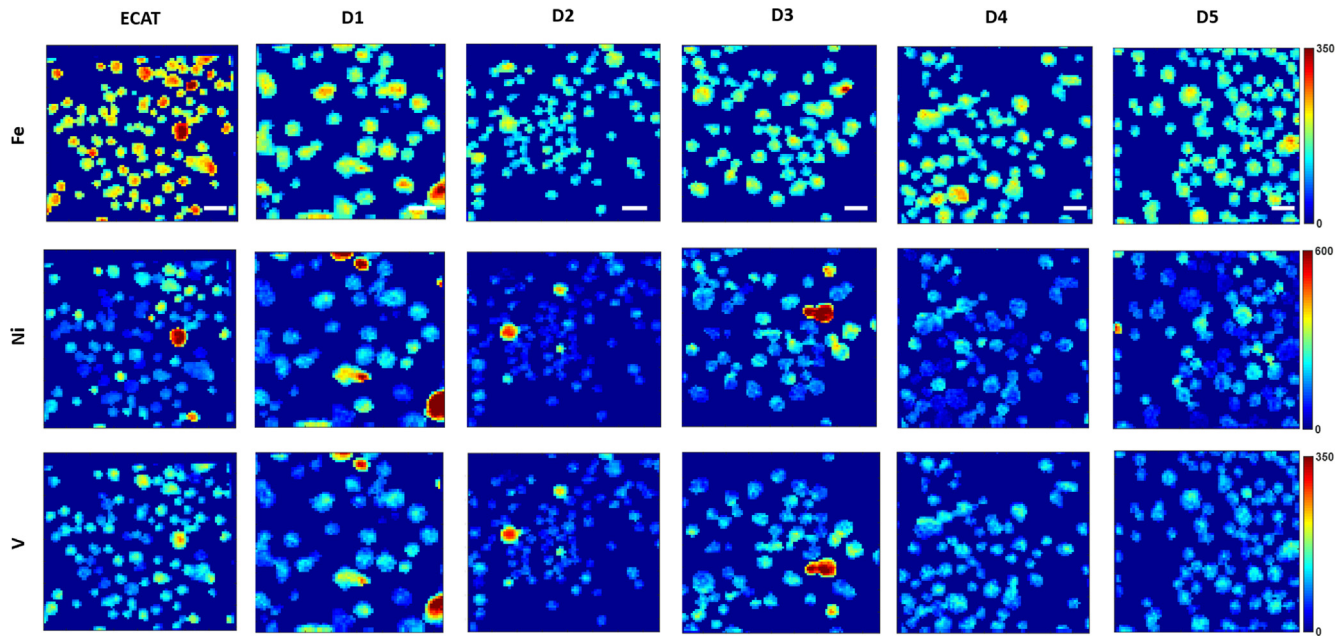

Fig. 4. Elemental distribution maps of Fe, Ni and V poisoning metals for the different DCATs samples, obtained after batch fitting analysis of the μXRF dataset. The scale bar indicates 150 μm.

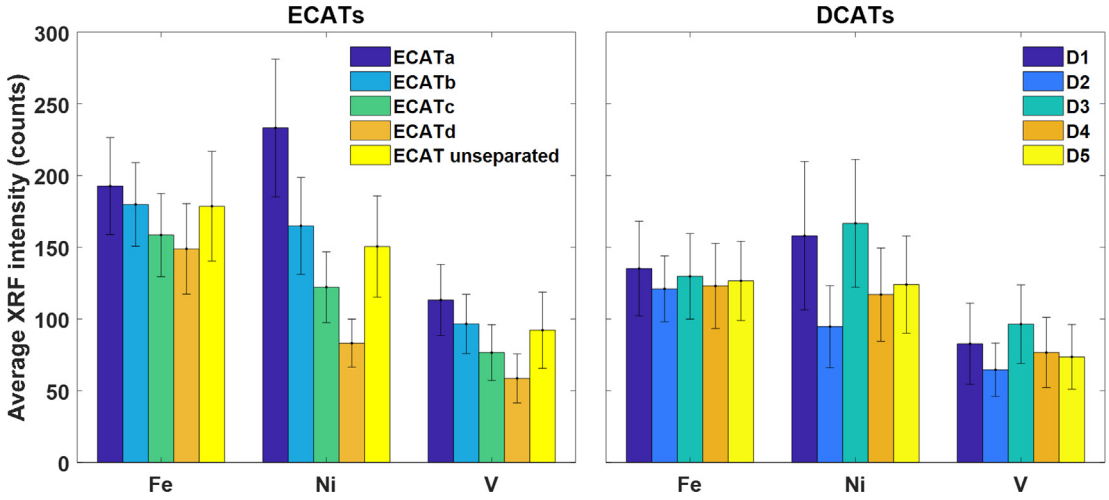

Fig. 5. Histogram distribution showing the average Fe, Ni, V poisoning metals content for the considered Region-of-Interest (ROI). The unseparated ECAT and density separated ECATa, ECATb, ECATc and ECATd data were published in ref. [18].

geneous distribution of Ni and V compared to the D1, D2 and D3 samples.

It can be therefore concluded that in terms of reproducing inter-particle heterogeneities (i.e., Ni and V hotspots) a combination of Mitchell impregnation and CPS seems to work better. However, this does not directly translate into a catalytic activity similar to the ECAT. We have previously shown that D5 has lower conversion than the other DCATs and it is similar to ECAT, suggesting that hydrothermal degradation conditions of the artificially deactivated samples are key to reproduce ECAT activity.

3.3. Phosphorus distribution

P has been used as a marker to evaluate the presence of additives in the considered FCC catalyst samples. Additives, containing zeolite ZSM-5 embedded in a mesoporous silica matrix, are used in the reactor to increase propylene yield during the catalytic cracking reaction.[23,24] P is usually added to ZSM-5-silica particles in order to aid the conversion of heavier molecules and it can therefore be used as a marker for locating these particles in the considered ROI. Fig. 6.**a** clearly shows that the fraction with the lowest skeletal density (i.e., the ECATd sample) contains the highest amount of additives (i.e., ~17% of all particles, as reported in Table 4). Fig. 6.**b** shows the overlay map of Nile Blue A (red) and P distribution (blue-green): it is evident that all the P-rich particles have very low Nile Blue A fluorescence, which is compatible with the reduced accessibility.

Synchrotron μXRD-μXRF tomography measurements of a particle selected from the ECATd fraction show the presence of the zeolite ZSM-5 phase, which is typical for FCC catalyst P-rich additives. Zeolite ZSM-5, Ni and Fe maps measured at around 18 μm depth are shown in Fig. 6.**c**. The average XRD patterns extracted over the virtual slices clearly show the presence of the zeolite ZSM-5 phase (Fig. 6.**d**), while no γ-alumina XRD peaks are visible. This

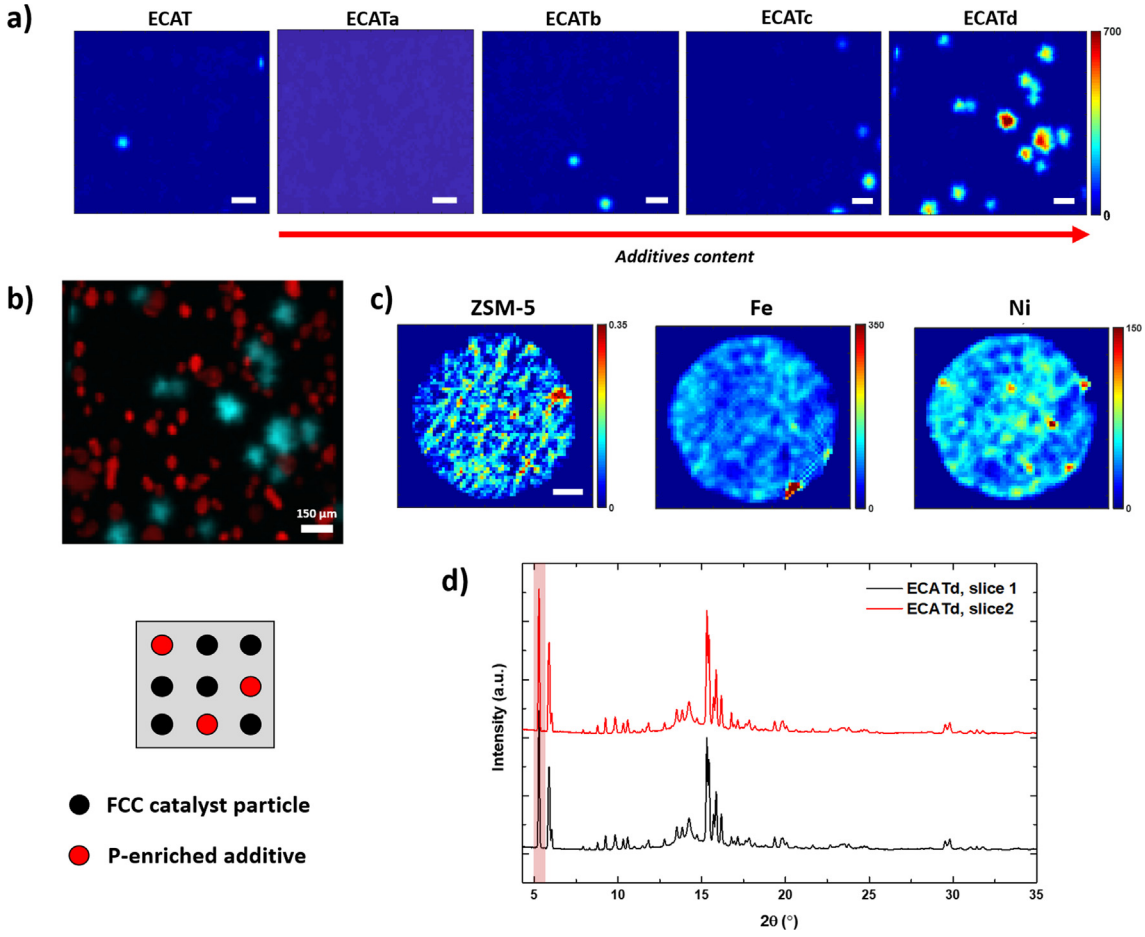

Fig. 6. a) P maps for the unseparated ECAT sample and for the ECAT density separated fractions. Scale bar is 150 µm. **b)** Overlay images of the registered Nile blue A (red) and P (blue-green) distribution maps of fraction ECATd. **c)** Single particle selected from ECATd batch: µXRD tomography measurements collected at SLS micro XAS beamline for slice 1 (18 µm depth) showing zeolite ZSM-5, Fe and Ni distribution (scale bar 10 µm). **d)** XRD pattern of particles taken from ECATd fraction measured at 18 µm (slice1) and 5 µm (slice2) depth. In the graph the XRD average pattern over different virtual slices is shown. The patterns show the presence of the zeolite ZSM-5 phase. The main ZSM-5 reflection is used to visualize the zeolite phase distribution and it is highlighted in the diffractogram. (For interpretation of the references to color in this figure legend, the reader is referred to the web version of this article.)

Table 4
Additive particles count, total number of particles and additives percentage for ECATs.

	Number of additive particles	Total number of particles	Additives percentage (%)
ECAT	2	92	2.17
ECATa	0	186	0.00
ECATb	2	135	1.48
ECATc	4	91	4.40
ECATd	15	88	17.05

is compatible with a different composition for these particles matrix, which is usually made of mesoporous silica.[45] This is also in line with the reduced accessibility of the P-containing particles. Furthermore, no additives are present in the DCATs samples.

3.4. Acidity and accessibility

The acidity and accessibility distribution for ECAT samples are reported in Fig. 7 **and S1.** Among the density sorted ECAT samples, the heaviest fraction (i.e., the ECATa sample) has reduced acidity and accessibility since it is composed by metal-rich aged FCC particles, that are highly deactivated. ECATb and ECATc have a broader acidity and accessibility range. The youngest fraction of the ECAT sample (i.e., ECATd) surprisingly shows lower acidity and accessibility. For this additive-rich fraction we can observe a high number of FCC particles showing lower accessibility (100 a.u.) that correspond to less accessible P-rich additive particles, that typically have a mesoporous silica matrix.

The acidity and accessibility distributions for the DCAT samples are shown in Fig. 8 **and S2.** The artificially deactivated FCC samples maintain a higher acidity as compared to the ECAT samples. It can also be noted that the accessibility in the DCAT samples is also higher as compared to the unseparated ECAT material. In order to rationalize these results several factors must be taken under consideration. Regarding acidity, it is well known that the decrease of Brønsted acid sites in the FCC catalyst is related to the dealumination of the embedded zeolite crystals, that occurs due to hydrothermal degradation over several catalytic cycles. This effect can be enhanced by the accumulation of V, that is known to form vanadic acid which has a destructive effect on the zeolite network. This aspect is very important to adequately reproduce FCC catalyst deactivation. Even though the Ni and V distribution is fairly well reproduced by the metalation artificial deactivation protocol in the D1, D2 and D3 samples, the fact that the acidity distribution is centered at a higher value than the ECAT samples suggests that the CPS samples were most probably not exposed to the same harsh regeneration conditions (i.e., high temperatures and presence of steam) as in the reactor. The higher acidity and accessibility

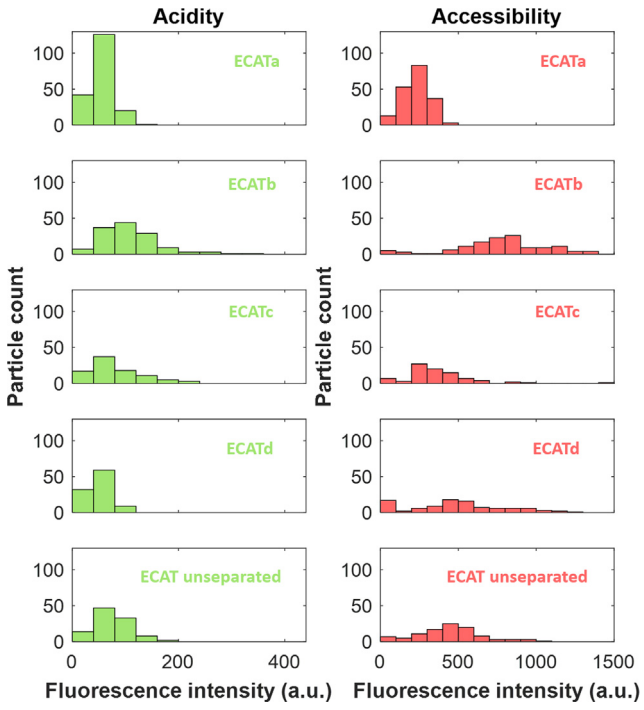

Fig. 7. Acidity and accessibility distribution respectively extracted from thiophene and Nile Blue A staining for the ECAT samples.

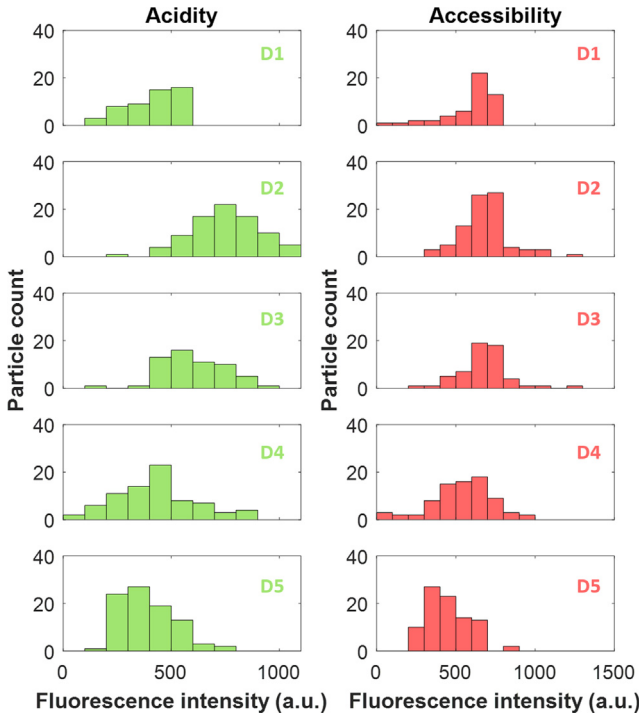

Fig. 8. Acidity and accessibility distribution respectively extracted from thiophene and Nile Blue A staining for the DCAT samples.

for DCAT samples when using these deactivation protocols compared to the ECAT is in line with literature findings.[27,30]

In order to explain the fact that the accessibility distribution is centered to higher values than for the ECATs, we look at the Fe distribution. In fact, as reported before, the DCAT samples have an average lower and more uniform Fe distribution compared to the ECAT samples. This strongly suggest the absence of Fe from external contamination, which is the one that had been linked to a pore clogging effect and surface vitrification in previous single particle studies.[10,46]

3.5. Correlation plots

A set of correlation plots related to metals distribution is reported in **Figs. S6 and S7**. If we look at the Pearson Correlation Coefficients (PCC), as reported in Fig. 9**,** for the ECAT samples and DCAT samples, we can immediately observe some differences. First of all, the Fe-Ni and Fe-V PCC are lower in the DCAT samples, most probably because the artificially deactivated samples all differ from the ECAT due to a lack of Fe external contamination, usually occurring from reactor components and to a less extent from feedstock. This is why an overall lower Fe-Ni and Fe-V correlation is observed compared to the ECATs.

Secondly, the Ni-V PCC are much higher (almost 1) for the D1, D2 and D3 samples. When comparing with the ECAT samples, these two elements are artificially added to the DCATs series via metalation and probably this difference in the correlation plot is related to a different interaction of these metals with the catalyst, that does not occur over several consecutive catalytic cycles.

Compared to previous studies, correlation plots of Fe-Ni, Fe-V and Ni-V (Figs. S6 and S7) give an interesting new insight on the effectiveness of the different artificial deactivation methods used to mimic ECAT deactivation. D1, that was deactivated through Mitchell impregnation followed by CPS shows higher similarity with the ECAT in terms of Ni and V distribution. However, as previously reported by Wallenstein et al.,[30] acidity and accessibility are higher compared to the ECAT.

The unseparated ECAT and its density sorted fractions show the same scattered trend of the Fe-Ni correlation plots, with PCC decreasing going from the metals-rich fraction ECATa to the metal-poor fraction ECATd. This trend is in line with the presence of less metals deactivated FCC particles following the order ECATd < ECATc < ECATb < ECATa. The more scattered trend of unseparated ECAT Fe-Ni correlation plot is compatible with the wider age distribution of the ECAT particles. If we compare these results with the DCAT series, it is evident that Fe-Ni correlation plot of D1 highly resembles to the unseparated ECAT one, having a similar linear scattered trend. The linear correlation is progressively lost going through the DCAT series, with a corresponding decrease in PCC (D5 < D4 < D3 < D2 < D1). From these results it can be concluded that metalation via Mitchell impregnation and CPS in D1 better mimic inter-particle heterogeneities and the presence on metals-rich particles of the ECAT compared to CD.

Regarding Fe-V correlation in the unseparated ECAT and its density sorted fractions, the PCC follows a similar trend as described for Fe-Ni. However, when we look at the DCAT series, some interesting results can be highlighted. Again, D1 is the sample that better mimics the unseparated ECAT scattered linear trend. D2 and D3 show lower correlation, while surprisingly CD-deactivated D4 and D5 show a linear trend which is much less scattered than the ECAT and D1, with higher PCC. The linear trend of CD deactivated D4 and D5 probably reflect a more uniform distribution of V among the particles and the higher Fe-V PCC, more similar to the ECAT, suggest a higher penetration of this metal through the particle, therefore being co-located with the Fe in the matrix.

Finally, Ni-V correlation plot in the ECATs, show the same scattered linear trend as the Fe-Ni and Fe-V correlation plots, with less PCC variations. However, in the DCATs series metalation/CPS deactivated D1, D2 and D3 show a strong linear trend and higher PCC compared to the unseparated ECAT. On the other side, CD-deactivated D4 and D5 have a lower Ni-V correlation. This suggests once more that samples deactivated through metalation and CPS

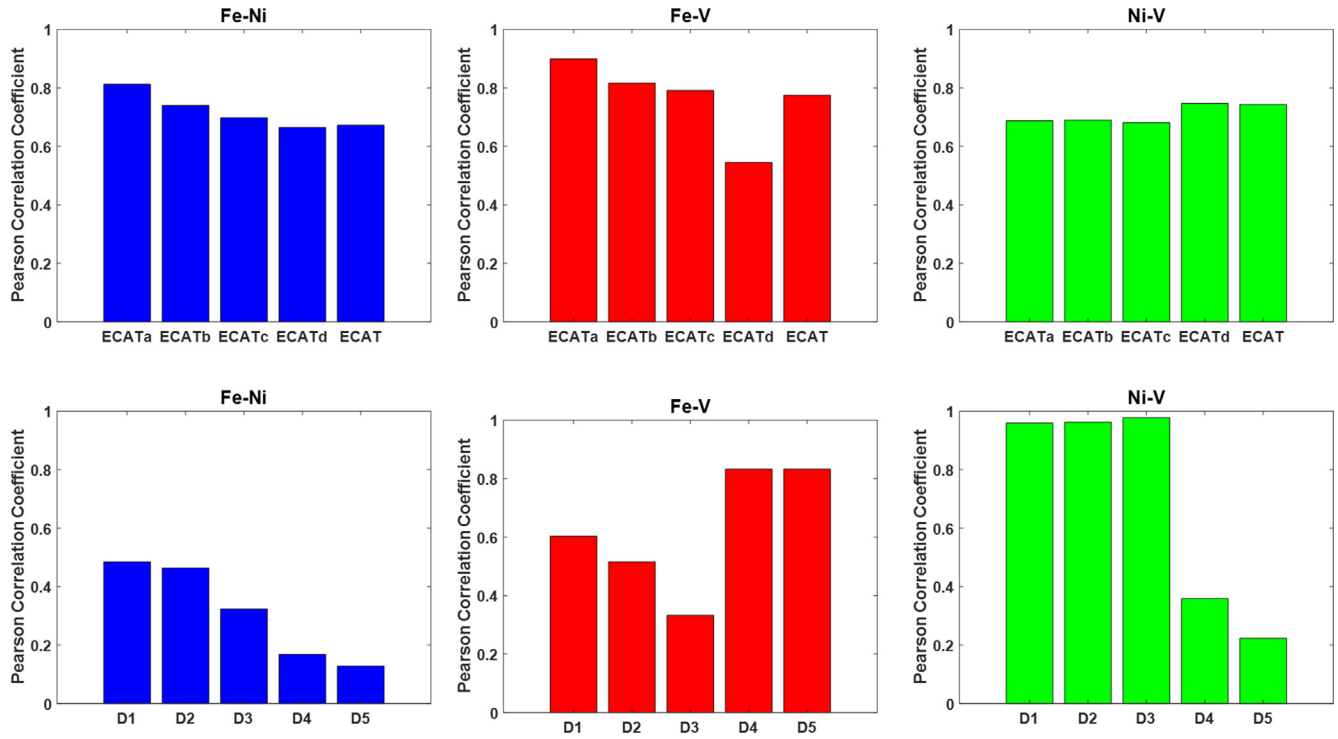

Fig. 9. The Pearson Correlation Coefficient (PCC) of the ECAT (top) and DCAT (bottom) samples for Fe-Ni, Fe-V and Ni-V.

have an inter-particle poisoning metals distribution that is more similar to the ECAT series compared to the CD deactivated samples. However, the less scattered trend of Ni-V correlation plot for D1, D2 and D3 compared to the ECAT, suggests that the simulation of inter-particle poisoning metals heterogeneity within the batch, and therefore the simulation of the age distribution of the ECAT, needs to be improved in the deactivation protocols.

It can be concluded that the Fe-Ni, Fe-V and Ni-V spatial correlations are very similar in the unseparated ECAT and D1 samples. In fact, D1 is the DCAT that is closer to the ECAT characteristics in terms of inter-particle metals distribution. Nevertheless, if we compare both acidity and accessibility, the D1 sample preserves a higher concentration of Brønsted acid sites as well as a higher accessibility compared to the ECAT sample. While the higher accessibility of the D1 sample can be related to the absence of additional Fe apart from that coming from the matrix, the higher acidity can be related to the catalyst treatment. We know that the drop in acidity is related to zeolite dealumination, that occurs over several regeneration cycles upon steam exposure. If the D1 sample was not exposed to the same average number of real-life regeneration cycles it is normal that it maintains a higher acidity. Also the Ni-V PCC, as explained before, remains higher in the D1 sample.

These results show that reproducing the poisoning metals distribution of the ECAT does not necessarily equal to obtain a catalyst that has similar acidity and accessibility properties, or similar catalytic performance. The relevance of mimicking the ECAT hydrothermal degradation seem to have a fundamental role in the success of a deactivation protocol.

4. Discussion

The comparison between the physicochemical and catalytic properties of the ECAT and DCAT catalysts helped us to better assess the effects of laboratory-based deactivation protocols. More specifically, we could evaluate different artificial aging processes in the riser-regenerator reactor system by evaluating the properties of the D1, D2 and D3, and D4 and D5 DCAT samples. In general, μXRF analysis highlighted a similarity in the Ni and V distribution between unseparated ECAT and D1 samples and the correlation plots also show a similar trend. Moving along the DCAT series, the D2 and D3 samples show progressively less similarity to the ECAT catalyst with very few metal hotspots, while the D4 and D5 samples have a lower and a more uniform Ni and V distribution. Though the Ni and V distribution is fairly reproduced in some of the artificially deactivated samples, Fe contamination is not taken into account. In fact, all DCAT catalysts have a uniform Fe distribution, indicating that the only Fe present in our samples is the one naturally contained in the clay. Based on previous single FCC catalyst particle studies, this can have an effect on the catalyst particle accessibility.

If we compare the unseparated ECAT catalyst with the DCAT materials, it can be clearly observed that the accessibility in DCATs remains always higher. This can be related to the absence in the DCAT samples of Fe contamination, that is known to cause pore clogging and vitrification on the particles surface. From the porosimetry data, reported in Table 1, it is evident that the total surface area (TSA) of the DCAT materials is higher or comparable than that of the ECAT sample. This observation is in line with the staining results. However, the larger differences in pore space arising from the porosity measurements are caused by the zeolite surface area (ZSA), while the matrix surface area (MSA) shows just small differences that perfectly reproduce the trend of our accessibility results, obtained via staining (compare e.g., Fig. 7, Fig. 8 and Table 1). In other words, Nile Blue A, the dye molecule to assess pore accessibility, can just diffuse into the matrix meso- and macropores and therefore it can be expected that our accessibility results reflect the MSA variations.

Regarding acidity, the histogram distribution in the DCAT catalysts is centered to higher values than in the ECAT catalyst. In fact, a very important parameter to reproduce acidity in the artificial deactivation protocol is hydrothermal degradation. Reproducing the high temperatures and the presence of steam in the reactor

over consecutive catalytic cycles is of utmost importance to accurately reproduce zeolite dealumination and therefore the related loss of Brønsted acidity in the laboratory-deactivated catalysts. If we take into consideration **Fig. S2**, the unseparated ECAT material has a very low acidity compared to the DCAT samples. Of course, we have just correlated this result to the ECAT higher exposure to hydrothermal degradation, but another reasoning can be put forward. It is well known that CFM is a technique that gives specific information on the confocal plane that is selected and that FCC catalyst particles show radial deactivation as they undergo industrial irreversible deactivation (i.e., poisoning metals deposition and hydrothermal degradation).[10] When we look at the unseparated ECAT acidity maps, there is a high chance that we are looking at a region of the particle that is part of this irreversibly deactivated radial volume. On the other hand, DCAT materials probably do not show this surface deactivation, at least the one related to the drop in acidity caused by hydrothermal degradation, and that is why we observe much higher acidity in these samples.

The fact that D1 metal distribution mimics fairly well the Ni and V inter-particle heterogeneities of the ECAT, does not translate in a similar behavior in terms of catalytic activity, where D5 shows more similarity to the ECAT in terms of conversion values. While D1 sample was deactivated with Mitchell impregnation and CPS, D5 was hydrothermally deactivated at 780 °C in 100% of steam for 32 h prior deactivation via CD-CPS: this strongly suggests that hydrothermal degradation plays a key role in the catalytic activity during fluid catalytic cracking.

Moreover, although we observe in D1 similar inter-particle Ni and V distribution, it would be interesting to use single particle correlative X-ray tomography methods (i.e., μXRF-μXRD- μXAS tomography) in order to characterize intra-particle heterogeneities in DCATs single particles and compare them to the ECAT: this would allow to check if artificially deactivated samples form secondary phases containing Ni and Al (i.e., nickel aluminate hotspots) that are present in the ECAT related to Ni-matrix interaction.[18] The absence of these hotspots, together with the absence of Fe from contamination and harsh hydrothermal condition might be the cause of the higher values of acidity and accessibility observed for the DCATs.

Finally, the density sorted ECAT materials helped to rationalize the effect of metal poisons on deactivation, especially in terms of the effect of Fe on the overall catalyst particle accessibility. Nevertheless, we must keep in mind that in the ECAT samples both metal poisoning and hydrothermal degradation are simultaneously present and build up over several catalysis-regeneration cycles. In the DCAT samples, although the metals distribution is well reproduced in some samples, the aging effect of hydrothermal degradation and the pore blocking effect of Fe are not as strongly reproduced as in the ECAT samples and a real age distribution is absent in the DCATs. Hence, this point requires further attention when developing alternative artificial aging protocols.

5. Conclusions

We have established, based on the previously developed method by Buurmans et al.[36] and Nieuwelink et al.[32], a generally applicable chemical staining protocol for multi-catalyst particle analysis that allows to validate artificial aging methods to simulate the industrial deactivation of Fluid Catalytic Cracking (FCC) materials. The strength of this protocol lies in the possibility to use different microscopy techniques in the same region of interest (ROI), therefore highlighting in a spatially resolved way inter-particle heterogeneities within FCC materials. This analytical approach allows a multiparticle microscopy analysis of solid catalysts that have been subjected to the staining of both thiophene and Nile Blue A, allowing to track acidity, accessibility and metals distribution in the same ROI. This approach will help future developments of laboratory-based deactivation protocols, which are essential in refinery industry for product evaluation and improvements.

Compared to the methods used in previous works, the strength of our analytical approach is in the possibility to track and correlate metals distribution, acidity and accessibility in a spatially resolved way in the same set of catalyst particles. This is not the case for bulk methods, such as FT-IR spectroscopy and diffusivity methods as they are not able to cope with spatiotemporal effects within a large batch of catalyst particles. Moreover, compared to SEM-EDS, this approach allows the fast screening of whole catalyst particles instead of cross sections, avoiding artifacts related to samples cut. However, our method does not provide sufficient resolution to assess intra-particle heterogeneities, that need to be further investigated using higher resolution single particle techniques (e.g., correlative X-ray tomography).

We have compared real-life industrially deactivated ECAT materials with artificially deactivated DCAT materials with the aim to assess the ability of different artificial deactivation protocols, more specifically metalation (Mitchell impregnation or spray impregnation) combined with Cyclic Propylene Steaming (CPS) and Cyclic Deactivation (CD) combined with CPS, to reproduce the characteristics of industrial FCC deactivation occurring in the riser-regenerator reactor unit over several catalytic cycles. We found that the exposure to real-life regeneration conditions is of utmost importance to reproduce the acidity drop in unseparated ECAT materials. Metalation/CPS deactivated samples reproduce slightly better certain ECAT characteristics, in particular spatial inter-particle heterogeneities in metal poisons, but do not mimic properly the catalytic activity of the ECAT, that is reproduced by the CD-CPS deactivated D5 sample, that was subjected to a harsh hydrothermally deactivation at 780 °C in 100% of steam for 32 h prior deactivation.

The absence of additional Fe (apart from the one present in the FCC catalyst matrix) in the artificially deactivated catalysts correlates with the higher accessibility in the DCAT materials compared to the unseparated ECAT sample and the ECATa fraction. The Ni-Fe, Ni-V and Fe-V XRF correlation plots showed spatial correlations for the ECAT materials. If we compare an unseparated ECAT sample with DCAT samples, we observe that going from fraction D1 to fraction D5 the observed linear correlation gradually decreases for the Ni-Fe and Ni-V pairs, as the amount of Ni and V hotspots decreases, while it increases for the Fe-V pair. Considering all findings, among the DCAT materials, the D1 fraction (subjected to metalation and CPS-aging) is the one showing most similarities with ECAT.

Finally, the developed correlative microscopy approach was effective for screening the presence of FCC particles, as well as additives containing zeolite ZSM-5, which are used as propylene production booster. By using the phosphorus maps as marker, we have found that the zeolite ZSM-5-containing FCC particles are more abundantly present in the lightest ECATd fraction of the density separated ECAT catalyst material.

Although the artificial protocols under analysis reproduce some of the main deactivation feature of the ECAT, deactivation methods need to be further improved in order to be able to fully mimic the complexity of an ECAT. Specifically, it will be necessary to address in the future the development of methods to simulate Fe deposition from reactor components, check the formation of nickel aluminates phases arising from metals-matrix interaction together with the zeolite degradation and dealumination occurring on the surface of the ECAT. The most challenging part of mimicking the ECAT, is reproducing via artificial protocols the age distribution

of an ECAT, simultaneously simulating metals deposition and hydrothermal degradation effects.

In order to achieve that, laboratory-based correlative microscopy inter-particle heterogeneities screening need to be integrated with higher resolution single particle methods, such as correlative X-ray tomography, that could map intra-particle heterogeneities related to metals deposition and hydrothermal degradation.

Declaration of Competing Interest

The authors declare that they have no known competing financial interests or personal relationships that could have appeared to influence the work reported in this paper.

Acknowledgements

This work was financially supported by Total, a VIDI grant to Florian Meirer from the Netherlands Organization for Scientific Research (NWO, no. 723.015.007) and a European Research Council (ERC) Advanced Grant to Bert M. Weckhuysen (grant number 321140). The authors thank Total for providing the FCC samples. We acknowledge the Swiss Light Source (SLS) for providing beamtime at microXAS X05LA beamline. We thank Marianne Maquet (Total) for performing the catalytic tests included in this study.

Appendix A. Supplementary material

Supplementary data to this article can be found online at https://doi.org/10.1016/j.jcat.2021.10.012.

References

[1] E.T.C. Vogt, B.M. Weckhuysen, Fluid catalytic cracking: recent developments on the grand old lady of zeolite catalysis, Chem. Soc. Rev. 44 (20) (2015) 7342–7370, https://doi.org/10.1039/C5CS00376H.
[2] M. Al-Sabawi, J. Chen, S. Ng, Fluid catalytic cracking of biomass-derived oils and their blends with petroleum feedstocks: a review, Energy Fuels 26 (9) (2012) 5355–5372, https://doi.org/10.1021/ef3006417.
[3] A.I. Hussain, A.M. Aitani, M. Kubů, J. Čejka, S. Al-Khattaf, Catalytic cracking of Arabian light VGO over novel zeolites as FCC catalyst additives for maximizing propylene yield, Fuel 167 (2016) 226–239, https://doi.org/10.1016/j.fuel.2015.11.065.
[4] D. Kubička, O. Kikhtyanin, Opportunities for zeolites in biomass upgrading—lessons from the refining and petrochemical industry, Catal. Today 243 (2015) 10–22, https://doi.org/10.1016/J.CATTOD.2014.07.043.
[5] J. Biswas, I.E. Maxwell, Recent process- and catalyst-related developments in fluid catalytic cracking, Appl. Catal. 63 (1990) 197–258.
[6] R.H. Harding, A.W. Peters, J.R.D. Nee, New developments in FCC catalyst technology, Appl. Catal. A Gen. 221 (1) (2001) 389–396, https://doi.org/10.1016/S0926-860X(01)00814-6.
[7] H.S. Cerqueira, G. Caeiro, L. Costa, F. Ramôa Ribeiro, Deactivation of FCC catalysts, J. Mol. Catal. A Chem. 292 (1) (2008) 1–13, https://doi.org/10.1016/j.molcata.2008.06.014.
[8] M. Niwa, K. Suzuki, K. Isamoto, N. Katada, Identification and measurements of strong brønsted acid site in Ultrastable Y (USY) zeolite, J. Phys. Chem. B 110 (1) (2006) 264–269, https://doi.org/10.1021/jp054442e.
[9] M. Falco, E. Morgado, N. Amadeo, U. Sedran, Accessibility in alumina matrices of FCC catalysts, Appl. Catal. A Gen. 315 (2006) 29–34, https://doi.org/10.1016/j.apcata.2006.08.028.
[10] F. Meirer, S. Kalirai, D. Morris, S. Soparawalla, Y. Liu, G. Mesu, J.C. Andrews, B. M. Weckhuysen, Life and death of a single catalytic cracking particle, Sci. Adv. 1 (3) (2015) 1:e400199, https://doi.org/10.1126/sciadv.1400199.
[11] F. Meirer, D.T. Morris, S. Kalirai, Y. Liu, J.C. Andrews, B.M. Weckhuysen, Mapping metals incorporation of a whole single catalyst particle using element specific X-ray nanotomography, J. Am. Chem. Soc. 137 (1) (2015) 102–105, https://doi.org/10.1021/ja511503d.
[12] A.M. Wise, J.N. Weker, S. Kalirai, M. Farmand, D.A. Shapiro, F. Meirer, B.M. Weckhuysen, Nanoscale chemical imaging of an individual catalyst particle with soft X-Ray ptychography, ACS Catal. 6 (4) (2016) 2178–2181, https://doi.org/10.1021/acscatal.6b00221.
[13] S. Kalirai, U. Boesenberg, G. Falkenberg, F. Meirer, B.M. Weckhuysen, X-ray fluorescence tomography of aged fluid-catalytic-cracking catalyst particles reveals insight into metal deposition processes, ChemCatChem 7 (22) (2015) 3674–3682, https://doi.org/10.1002/cctc.201500710.
[14] Y. Liu, F. Meirer, C.M. Krest, S. Webb, B.M. Weckhuysen, Relating structure and composition with accessibility of a single catalyst particle using correlative 3-dimensional micro-spectroscopy, Nat. Commun. 7 (2016) 12634.
[15] J. Ihli, D. Ferreira Sanchez, R.R. Jacob, V. Cuartero, O. Mathon, F. Krumeich, C. Borca, T. Huthwelker, W.-C. Cheng, YuYing Shu, S. Pascarelli, D. Grolimund, A. Menzel, J.A. van Bokhoven, Localization and speciation of iron impurities within a fluid catalytic cracking catalyst, Angew. Chem. 129 (45) (2017) 14219–14223, https://doi.org/10.1002/ange.201707154.
[16] F. Krumeich, J. Ihli, YuYing Shu, W.-C. Cheng, J.A. van Bokhoven, Structural changes in deactivated fluid catalytic cracking catalysts determined by electron microscopy, ACS Catal. 8 (5) (2018) 4591–4599, https://doi.org/10.1021/acscatal.8b0064910.1021/acscatal.8b00649.s001.
[17] N.L.A. Souza, R. Paniago, J.D. Ardisson, E. Morgado, K. Krambrock, Iron contamination of FCC catalysts: quantification of different crystalline phases and valence states, Appl. Catal. A Gen. 569 (2019) 57–65, https://doi.org/10.1016/j.apcata.2018.10.019.
[18] M. Gambino, M. Veselý, M. Filez, R. Oord, D. Ferreira Sanchez, D. Grolimund, N. Nesterenko, D. Minoux, M. Maquet, F. Meirer, B.M. Weckhuysen, Nickel poisoning of a cracking catalyst unravelled by single-particle X-ray fluorescence-diffraction-absorption tomography, Angew. Chem. Int. Ed. 59 (10) (2020) 3922–3927, https://doi.org/10.1002/anie.v59.1010.1002/anie.201914950.
[19] J. Ihli, R.R. Jacob, M. Holler, M. Guizar-Sicairos, A. Diaz, J.C. da Silva, D. Ferreira Sanchez, F. Krumeich, D. Grolimund, M. Taddei, W.-C. Cheng, Y. Shu, A. Menzel, J.A. van Bokhoven, A three-dimensional view of structural changes caused by deactivation of fluid catalytic cracking catalysts, Nat. Commun. 8 (2017) 809, https://doi.org/10.1038/s41467-017-00789-w.
[20] J. Ihli, A. Diaz, Y. Shu, M. Guizar-Sicairos, M. Holler, K. Wakonig, M. Odstrcil, T. Li, F. Krumeich, E. Müller, W.-C. Cheng, J.A. van Bokhoven, A. Menzel, Resonant ptychographic tomography facilitates three-dimensional quantitative colocalization of catalyst components and chemical elements, J. Phys. Chem. C 122 (40) (2018) 22920–22929, https://doi.org/10.1021/acs.jpcc.8b05624.s005.
[21] H. Jiang, Silicon enrichment on iron contaminated fluid catalytic cracking catalyst particle surface, J. Catal. 382 (2020) 31–39, https://doi.org/10.1016/j.jcat.2019.12.013.
[22] A.A. Lappas, L. Nalbandian, D.K. Iatridis, S.S. Voutetakis, I.A. Vasalos, Effect of metals poisoning on FCC products yields: studies in an FCC short contact time pilot plant unit, Catal. Today 65 (2) (2001) 233–240, https://doi.org/10.1016/S0920-5861(00)00588-5.
[23] Y. Sang, H. Li, Effect of phosphorus and mesopore modification on the HZSM-5 zeolites for n-decane cracking, J. Solid State Chem. 271 (2019) 326–333, https://doi.org/10.1016/j.jssc.2019.01.016.
[24] Y. Ji, H. Yang, W. Yan, Strategies to enhance the catalytic performance of ZSM-5 zeolite in hydrocarbon cracking: a review, Catalysts 7 (12) (2017) 367.
[25] M. Bendiksen, E. Tangstad, T. Myrstad, A comparison of laboratory deactivation methods for FCC catalysts, Appl. Catal. A Gen. 129 (1) (1995) 21–31.
[26] B.R. Mitchell, Metal contamination of cracking catalysts. 1. Synthetic metals deposition on fresh catalysts, Ind. Eng. Chem. Prod. Res. Dev. 19 (2) (1980) 209–213.
[27] A.C. Psarras, E.F. Iliopoulou, K. Kostaras, A.A. Lappas, C. Pouwels, Investigation of advanced laboratory deactivation techniques of FCC catalysts via FTIR acidity studies, Microporous Mesoporous Mater. 120 (1–2) (2009) 141–146.
[28] R. Sadeghbeigi, Fluid Catalytic Cracking Handbook: An Expert Guide to the Practical Operation, Design, and Optimization of FCC Units, Elsevier, Amsterdam, 2012.
[29] D. Wallenstein, T. Roberie, T. Bruhin, Review on the deactivation of FCC catalysts by cyclic propylene steaming, Catal. Today 127 (1–4) (2007) 54–69, https://doi.org/10.1016/j.cattod.2007.05.023.
[30] D. Wallenstein, D. Farmer, J. Knoell, C.M. Fougret, S. Brandt, Progress in the deactivation of metals contaminated FCC catalysts by a novel catalyst metallation method, Appl. Catal. A Gen. 462–463 (2013) 91–99, https://doi.org/10.1016/j.apcata.2013.02.002.
[31] A.C. Psarras, E.F. Iliopoulou, L. Nalbandian, A.A. Lappas, C. Pouwels, Study of the accessibility effect on the irreversible deactivation of FCC catalysts from contaminant feed metals, Catal. Today 127 (1) (2007) 44–53, https://doi.org/10.1016/j.cattod.2007.05.021.
[32] A.E. Nieuwelink, M.E.Z. Velthoen, Y.C.M. Nederstigt, K.L. Jagtenberg, F. Meirer, B.M. Weckhuysen, Single particle essays to determine heterogeneities within fluid catalytic cracking catalysts, Chem. Eur. J. 26 (2020) 8546–8554, https://doi.org/10.1002/chem.201905880.
[33] J. Zhang, R.E. Campbell, A.Y. Ting, R.Y. Tsien, Creating new fluorescent probes for cell biology, Nat. Rev. Mol. cell Biol. 3 (12) (2002) 906–918.
[34] B.M. Weckhuysen, Solid catalysts under the spotlight, Nat. Catal. 1 (2) (2018) 101–102, https://doi.org/10.1038/s41929-018-0024-6.
[35] I.L.C. Buurmans, B.M. Weckhuysen, Heterogeneities of individual catalyst particles in space and time as monitored by spectroscopy, Nat. Chem. 4 (2012) 873–886.
[36] I.L.C. Buurmans, J. Ruiz-Martínez, W.V. Knowles, D. van der Beek, J.A. Bergwerff, E.T.C. Vogt, B.M. Weckhuysen, Catalytic activity in individual cracking catalyst particles imaged throughout different life stages by selective staining, Nat. Chem. 3 (2011) 862–867.
[37] I.L.C. Buurmans, E.A. Pidko, J.M. de Groot, E. Stavitski, R.A. van Santen, B.M. Weckhuysen, Styrene oligomerization as a molecular probe reaction for zeolite acidity: a UV-Vis spectroscopy and DFT study, Phys. Chem. Chem. Phys. 12 (26) (2010) 7032–7040.

[38] I.L.C. Buurmans, J. Ruiz-Martinez, S.L. van Leeuwen, D. van der Beek, J.A. Bergwerff, W.V. Knowles, E.T.C. Vogt, B.M. Weckhuysen, Staining of fluid-catalytic-cracking catalysts: localising brønsted acidity within a single catalyst particle, Chem. Eur. J. 18 (4) (2012) 1094–1101.
[39] M.A. Karreman, I.L.C. Buurmans, J.W. Geus, A.V. Agronskaia, J. Ruiz-Martínez, H.C. Gerritsen, B.M. Weckhuysen, Integrated laser and electron microscopy correlates structure of fluid catalytic cracking particles to brønsted acidity, Angew. Chem. Int. Ed. 51 (6) (2012) 1428–1431.
[40] M. Solsona, A.-E. Nieuwelink, F. Meirer, L. Abelmann, M. Odijk, W. Olthuis, B.M. Weckhuysen, A. van den Berg, Magnetophoretic sorting of single catalyst particles, Angew. Chem. Int. Ed. 57 (33) (2018) 10589–10594.
[41] M.A. Karreman, I.L.C. Buurmans, A.V. Agronskaia, J.W. Geus, H.C. Gerritsen, B.M. Weckhuysen, Probing the different life stages of a fluid catalytic cracking particle with integrated laser and electron microscopy, Chem. Eur. J. 19 (12) (2013) 3846–3859, https://doi.org/10.1002/chem.201203491.
[42] Z. Ristanović, M.M. Kerssens, A.V. Kubarev, F.C. Hendriks, P. Dedecker, J. Hofkens, M.B.J. Roeffaers, B.M. Weckhuysen, High-resolution single-molecule fluorescence imaging of zeolite aggregates within real-life fluid catalytic cracking particles, Angew. Chem. Int. Ed. 54 (6) (2015) 1836–1840, https://doi.org/10.1002/anie.201410236.
[43] J.C. Kayser, Versatile Fluidized Bed Reactor, U.S. Patent 6,069,012, 2000.
[44] V.A. Solé, E. Papillon, M. Cotte, Ph. Walter, J. Susini, A multiplatform code for the analysis of energy-dispersive X-ray fluorescence spectra, Spectrochim. Acta Part B 62 (1) (2007) 63–68.
[45] B.R. Jermy, M.A.B. Siddiqui, A.M. Aitani, M.R. Saeed, S. Al-Khattaf, Utilization of ZSM-5/MCM-41 composite as FCC catalyst additive for enhancing propylene yield from VGO cracking, J. Porous Mater. 19 (4) (2012) 499–509.
[46] F. Meirer, S. Kalirai, J. Nelson-Weker, Y. Liu, J.C. Andrews, B.M. Weckhuysen, Agglutination of single catalyst particles during fluid catalytic cracking as observed by X-ray nanotomography, Chem. Commun. 51 (38) (2015) 8097–8100, https://doi.org/10.1039/C5CC00401B.